Inorg. Chem. **2005**, *44*, 9795–9806

Magnetism, Electron Paramagnetic Resonance, Electrochemistry, and Mass Spectrometry of the Pentacopper(II)-Substituted Tungstosilicate $[Cu_5(OH)_4(H_2O)_2(A\text{-}\alpha\text{-}SiW_9O_{33})_2]^{10-}$, A Model Five-Spin Frustrated Cluster

Saritha Nellutla,[†] Johan van Tol,[†] Naresh S. Dalal,*[,†] Li-Hua Bi,[‡] Ulrich Kortz,*[,‡] Bineta Keita,[§] Louis Nadjo,*[,§] Gregory A. Khitrov,[†] and Alan G. Marshall*[,†]

Department of Chemistry and Biochemistry, Florida State University, and National High Magnetic Field Laboratory and Center for Interdisciplinary Magnetic Resonance, Tallahassee, Florida 32306-4390, School of Engineering and Science, International University Bremen, P.O. Box 750 561, 28725 Bremen, Germany, and Laboratoire de Chimie Physique, UMR 8000, CNRS, Equipe d'Electrochimie et Photoélectrochimie, Université Paris-Sud, Bâtiment 420, 91405 Orsay Cedex, France

Received July 27, 2005

The dimeric, pentacopper(II)-substituted tungstosilicate $[Cu_5(OH)_4(H_2O)_2(A\text{-}\alpha\text{-}SiW_9O_{33})_2]^{10-}$ (**1**) has been characterized by single-crystal X-ray diffraction, elemental analysis, IR, electrochemistry, magnetic measurements, electron paramagnetic resonance (EPR), and mass spectrometry (MS). Magnetization and high-field EPR measurements reveal that the pentameric copper core $\{Cu_5(OH)_4(H_2O)_2\}^{6+}$ of **1** exhibits strong antiferromagnetic interactions ($J_a = -51 \pm 6$ cm^{-1}, $J_b = -104 \pm 1$ cm^{-1}, and $J_c = -55 \pm 3$ cm^{-1}) resulting in a spin $S_T = {}^1/_2$ ground state. EPR data show that the unpaired electron spin density is localized on the spin-frustrated apical Cu^{2+} ion with $g_{zz} = 2.4073 \pm 0.0005$, $g_{yy} = 2.0672 \pm 0.0005$, $g_{xx} = 2.0240 \pm 0.0005$, and $A_{zz} = -340 \pm 20$ MHz (–0.0113 cm^{-1}). **1** can therefore be considered as a model system for a five-spin, electronically coupled, spin-frustrated system. Polyanion **1**, which is stable over a wide pH domain (pH 1–7), was characterized by cyclic voltammetry (CV) in a pH 5 medium. Its CV was constituted by an initial two-step reduction of the Cu^{2+} centers to Cu^0 through Cu^+, followed at more negative potential by the redox processes of the W centers. Controlled potential coulometry of **1** allows for the reduction of the five Cu^{2+} centers, as seen by consumption of 10.05 ± 0.05 electrons per molecule. Polyanion **1** triggers efficiently the electrocatalytic reduction of nitrate and nitrite, and it also catalyzes the reduction of N_2O. To our knowledge, this is the first example of N_2O catalytic reduction by a polyoxoanion. Fourier transform ion cyclotron resonance MS was used to unambiguously assign the molecular weight of the solution-phase species **1** and the oxidation states of the Cu atoms in the central $\{Cu_5(OH)_4(H_2O)_2\}^{6+}$ core. Infrared (IR) multiphoton dissociation MS/MS of **1** showed evidence of a condensation process similar to bronze formation at low irradiation intensity. Higher IR intensity resulted in the formation of stable fragments consistent with those previously observed in the solution chemistry of polyoxoanions.

Introduction

Polyoxometalates (POMs) are metal−oxygen cluster species with a diverse compositional range and an enormous structural variety.[1−6] Although the class of POMs has been known for about 200 years, the mechanism of formation of POMs is not well understood and is commonly described as self-assembly. Therefore, the systematic structural design of novel POMs and the derivatization of known POMs remain challenges for synthetic chemists.

* To whom correspondence should be addressed. E-mail: dalal@chemmail.chem.fsu.edu (N.S.D.), u.kortz@iu-bremen.de (U.K.), louis.nadjo@lcp.u-psud.fr (L.N.), marshall@magnet.fsu.edu (A.G.M.). Fax: (+49)421-200 3229 (U.K.), (+1)850-644 3398 (N.S.D.).

[†] Department of Chemistry and Biochemistry, Florida State University, and National High Magnetic Field Laboratory and Center for Interdisciplinary Magnetic Resonance.

[‡] International University Bremen.

[§] Université Paris-Sud.

(1) Pope, M. T. *Heteropoly and Isopoly Oxometalates*; Springer-Verlag: Berlin, 1983.
(2) Pope, M. T.; Müller, A. *Angew. Chem., Int. Ed. Engl.* **1991**, *30*, 34.
(3) *Polyoxometalates: From Platonic Solids to Anti-Retroviral Activity*; Pope, M. T., Müller, A., Eds.; Kluwer: Dordrecht, The Netherlands, 1994.

10.1021/ic0512633 CCC: $30.25
Published on Web 11/17/2005

Transitional-metal-substituted POMs (TMSPs) have attracted increasing attention in recent years because of their highly tunable nature, coupled with their fascinating properties, resulting in potential applications in catalysis, material science, and medicine.[7−10] Within the class of TMSPs, the sandwich-type compounds represent the largest subclass.[7,11] To date, the Weakley-, Hervé-, Krebs-, and Knoth-type sandwich polyanions can be distinguished. However, considering that formation of polyanions occurs via self-assembly, the discovery of novel TMSPs with fundamentally novel structures continues to be a focus of considerable ongoing research. These synthetic efforts are often accompanied by attempts to incorporate a large number of paramagnetic transition-metal ions in lacunary polyanion fragments, to obtain products with interesting magnetic and/or redox properties.

The class of Cu^{2+}-containing, sandwich-type POMs is well-known, and to date, numerous complexes have been reported. Most of these polyanions are dimeric and contain three or four Cu^{2+} centers, e.g., $[Cu_3(H_2O)_3(XW_9O_{33})_2]^{12-}$ ($X = As^{III}$, Sb^{III}), $[Cu_4(H_2O)_2(XW_9O_{34})_2]^{n-}$ ($X = P^{V}$, As^{V}, $n = 10$; $X = Si^{IV}$, $n = 12$).[12] In 2004, we reported on the synthesis and magnetic properties of the tetracopper(II)-substituted tungstoarsenate(III) $[Cu_4K_2(H_2O)_8(\alpha\text{-}AsW_9O_{33})_2]^{8-}$.[13] The year before, Mialane et al. described the tetrameric Cu_{14}-containing tungstosilicate.[14] Very recently, we reported on the wheel-shaped eicosacopper tungstophosphate $[Cu_{20}Cl(OH)_{24}(H_2O)_{12}(P_8W_{48}O_{184})]^{25-}$, which contains more Cu^{2+} ions than any other POM to date.[15]

Late last year, two of us communicated the synthesis and structure of the pentacopper(II)-substituted polyoxoanion $[Cu_5(OH)_4(H_2O)_2(A\text{-}\alpha\text{-}SiW_9O_{33})_2]^{10-}$.[16] In this paper, we report on the magnetic susceptibility, electron paramagnetic resonance, redox behavior (electrochemistry), elemental composition, metal charge state, and thermal fragmentation by ultrahigh-resolution mass spectrometry of $[Cu_5(OH)_4(H_2O)_2(A\text{-}\alpha\text{-}SiW_9O_{33})_2]^{10-}$.

Table 1. Crystal Data and Structure Refinement for **K-1**

empirical formula	$Cu_5H_{45}K_{10}O_{90.5}Si_2W_{18}$
fw	5567.6
space group	$P\bar{1}$ (No. 2)
a (Å)	13.4108(7)
b (Å)	15.5496(8)
c (Å)	24.1156(12)
α (deg)	100.0840(10)
β (deg)	101.9270(10)
γ (deg)	103.3990(10)
V (Å^3)	4653.2(4)
Z	2
T (°C)	−100
wavelength (Å)	0.71073
d_{calcd} (Mg m^{-3})	3.823
abs coeff (mm^{-1})	23.653
R [$I > 2\sigma(I)$][a]	0.069
R_w (all data)[b]	0.179

[a] $R = \sum||F_o| - |F_c||/\sum|F_o|$. [b] $R_w = [\sum w(F_o^2 - F_c^2)^2/\sum w(F_o^2)^2]^{1/2}$.

Experimental Setup

Synthesis. All reagents were used as purchased without further purification. The trilacunary precursor $K_{10}[A\text{-}\alpha\text{-}SiW_9O_{34}]$ was synthesized according to the published procedure.[17]

$K_{10}[Cu_5(OH)_4(H_2O)_2(A\text{-}\alpha\text{-}SiW_9O_{33})_2]\cdot 18.5H_2O$ (K-1). A 0.50-g (0.16-mmol) sample of $K_{10}[A\text{-}\alpha\text{-}SiW_9O_{34}]$ was added with stirring to a solution of 0.076 g (0.44 mmol) of $CuCl_2\cdot 2H_2O$ in 20 mL of a 0.5 M NaAc buffer (pH 4.8). This solution was heated to 80 °C for 30 min and then cooled to room temperature and filtered. Slow evaporation at room temperature resulted after about 1−2 weeks in green crystals that were filtered off and air-dried. Yield: 0.28 g (63%). IR for **K-1**: 1008, 945, 915, 885, 810, 768, 698, 595, 546, 524 cm^{-1}. Anal. Calcd (found) for **K-1**: K, 7.0 (7.2); Cu, 5.7 (5.6); W, 59.4 (59.8); Si, 1.0 (1.1). Elemental analysis was performed by Kanti Labs Ltd. in Mississauga, Canada.

X-ray Crystallography. A light-green block of **K-1** with dimensions 0.20 × 0.20 × 0.16 mm^3 was mounted on a glass fiber for indexing and intensity data collection at 173 K with a Bruker D8 SMART APEX CCD single-crystal diffractometer by use of Mo Kα radiation ($\lambda = 0.710\ 73$ Å). Of the 22 732 unique reflections ($2\theta_{max} = 56.56°$), 19 331 reflections ($R_{int} = 0.033$) were considered observed [$I > 2\sigma(I)$]. Direct methods were used to solve the structure and to locate the tungsten and copper atoms (*SHELXS-97*). Then the remaining atoms were found from successive difference maps (*SHELXL-97*). The final cycle of refinement, including the atomic coordinates, anisotropic thermal parameters (W, Cu, Si, and K atoms), and isotropic thermal parameters (O atoms), converged at $R = 0.069$ and $R_w = 0.179$ [$I > 2\sigma(I)$]. In the final difference map, the deepest hole was −2.184 e Å^{-3} and the highest peak 4.938 e Å^{-3}. Routine Lorentz and polarization corrections were applied, and an absorption correction was performed with the *SADABS* program.[18] Crystallographic data are summarized in Table 1.

Magnetic Measurements. Magnetic susceptibility measurements were carried out on compacted powder samples from 1.8 to 300 K at an external field of 0.1 T with a Quantum Design MPMS SQUID magnetometer. The data were corrected for diamagnetism

(4) Polyoxometalates. In *Chemical Reviews*; Hill, C., Ed.; American Chemical Society: Washington, DC, 1998.
(5) *Polyoxometalate Chemistry: From Topology via Self-Assembly to Applications*; Pope, M. T., Müller, A., Eds.; Kluwer: Dordrecht, The Netherlands, 2001.
(6) *Polyoxometalate Chemistry for Nano-Composite Design*; Yamase, T., Pope, M. T., Eds.; Kluwer: Dordrecht, The Netherlands, 2002.
(7) Pope, M. T. *Comput. Coord. Chem. II* **2003**, *4*, 635.
(8) Hill, C. L. *Comput. Coord. Chem. II* **2003**, *4*, 679.
(9) *Polyoxometalate Molecular Science*; Borrás-Almenar, J. J., Coronado, E., Müller, A., Pope, M. T., Eds.; Kluwer: Dordrecht, The Netherlands, 2004.
(10) Casan-Pastor, N.; Gomez-Romero, P. *Front. Biosci.* **2004**, *9*, 1759.
(11) Representative references include: (a) Bi, L.-H.; Kortz, U.; Keita, B.; Nadjo, L.; Daniels, L. *Eur. J. Inorg. Chem.* **2005**, 3034. (b) Kortz, U.; Nellutla, S.; Stowe, A. C.; Dalal, N. S.; Rauwald, U.; Danquah, W.; Ravot, D. *Inorg. Chem.* **2004**, *43*, 2308. (c) Mbomekalle, I. M.; Keita, B.; Nadjo, L.; Hardcastle, K. I.; Hill, C. L.; Anderson, T. M. *Dalton Trans.* **2004**, 4094. (d) Yamase, T.; Ishikawa, E.; Fukaya, K.; Nojiri, H.; Taniguchi, T.; Atake, T. *Inorg. Chem.* **2004**, *43*, 8150.
(12) (a) Kortz, U.; Al-Kassem, N. K.; Savelieff, M. G.; Al Kadi, N. A.; Sadakane, M. *Inorg. Chem.* **2001**, *40*, 4742. (b) Weakley, T. J. R.; Finke, R. G. *Inorg. Chem.* **1990**, *29*, 1235. (c) Bi, L.-H.; Huang, R.-D.; Peng, J.; Wang, E.-B.; Wang, Y. H.; Hu, C.-W. *J. Chem. Soc., Dalton Trans.* **2001**, 121. (d) Kortz, U.; Isber, S.; Dickman, M. H.; Ravot, D. *Inorg. Chem.* **2000**, *39*, 2915.
(13) Kortz, U.; Nellutla, S.; Stowe, A. C.; Dalal, N. S.; van Tol, J.; Bassil, B. S. *Inorg. Chem.* **2004**, *43*, 144.
(14) Mialane, P.; Dolbecq, A.; Marrot, J.; Rivière, E.; Sécheresse, F. *Angew. Chem., Int. Ed.* **2003**, *42*, 3523.
(15) (a) Mal, S. S.; Kortz, U. *Angew. Chem., Int. Ed.* **2005**, *44*, 3777. (b) Jabbour, D.; Keita, B.; Nadjo, L.; Kortz, U.; Mal, S. S. *Electrochem. Commun.* **2005**, *7*, 841.
(16) Bi, L.-H.; Kortz, U. *Inorg. Chem.* **2004**, *43*, 7961.
(17) Laronze, N.; Marrot, J.; Hervé, G. *Inorg. Chem.* **2003**, *42*, 5857.
(18) Sheldrick, G. M. *SADABS*; Siemens Analytical X-ray Instrument Division: Madison, WI, 1995.

estimated from Klemm constants and temperature-independent paramagnetism of the Cu^{2+} ions.[19]

EPR Measurements. Polycrystalline powder EPR spectra were recorded at frequencies ranging from 34 to 190 GHz and in the temperature range 4−300 K. A Bruker Elexsys-500 spectrometer was used for Q-band (ν = 34 GHz) measurements, whereas the high-frequency measurements were conducted with a custom-built variable-frequency EPR spectrometer at the National High Magnetic Field Laboratory in Tallahassee, FL.[20] All experimental spectra were simulated with locally developed computer programs.

Electrochemical Methods and Materials. Pure water was used throughout. It was obtained by passage through a RiOs 8 unit followed by a Millipore-Q Academic purification set. All reagents were of high-purity grade and were used as purchased without further purification. The compositions of the various media were as follows: for pH 3, 0.2 M Na_2SO_4 + H_2SO_4; for pH 5, 0.4 M CH_3COONa + CH_3COOH.

Electrochemical Experiments. The polyanion concentration was 2×10^{-4} M. The solutions were deaerated thoroughly for at least 30 min with pure argon and kept under a positive pressure of this gas during the experiments. The source, mounting, and polishing of the glassy carbon (GC; Tokai, Japan) electrodes has been described.[21] The GC samples had a diameter of 3 mm. The electrochemical apparatus was an EG&G 273 A driven by a PC with M270 software. Potentials are referred to a saturated calomel electrode (SCE). The counter electrode was a platinum gauze of large surface area. All experiments were performed at room temperature.

MS. Polyanion $[Cu_5(OH)_4(H_2O)_2(A\text{-}\alpha\text{-}SiW_9O_{33})_2]^{10-}$ (**1**) was isolated as an *n*-tetrabutylammonium (TBA) salt by the addition of solid TBABr to a solution of **1**[16] followed by washing with H_2O. Then the product was isolated by suction filtration and air-dried. For MS analysis, a micromolar solution of **1** in acetonitrile (Fisher) was infused, at 300 nL/min, into the microelectrospray source of a home-built 9.4-T Fourier transform ion cyclotron resonance (FT-ICR) instrument configured for mass-selective external ion accumulation.[22] For MS/MS, the desired parent ion was isolated by external quadrupole mass filtering and irradiation in the ICR cell with a 40-W continuous-wave CO_2 laser (Synrad, Mukilteo, WA) to induce dissociation.

Results and Discussion

Synthesis and Structure. The dimeric title polyanion **1** consists of two A-α-$[SiW_9O_{34}]^{10-}$ Keggin moieties that are linked via two adjacent W−O−W bonds and stabilized by a central $\{Cu_5(OH)_4(H_2O)_2\}^{6+}$ fragment, leading to a structure with idealized C_{2v} symmetry (see Figure 1a).[16] Polyanion **1** is stable over a very wide pH range (pH 1−7), as shown by UV−vis and IR. The structure of **1** can also be visualized as an open Wells−Dawson polyanion $[Si_2W_{18}O_{66}]^{16-}$ (first reported by Hervé and co-workers),[23] which has taken up the cationic copper−oxo cluster $\{Cu_5(OH)_4(H_2O)_2\}^{6+}$. The

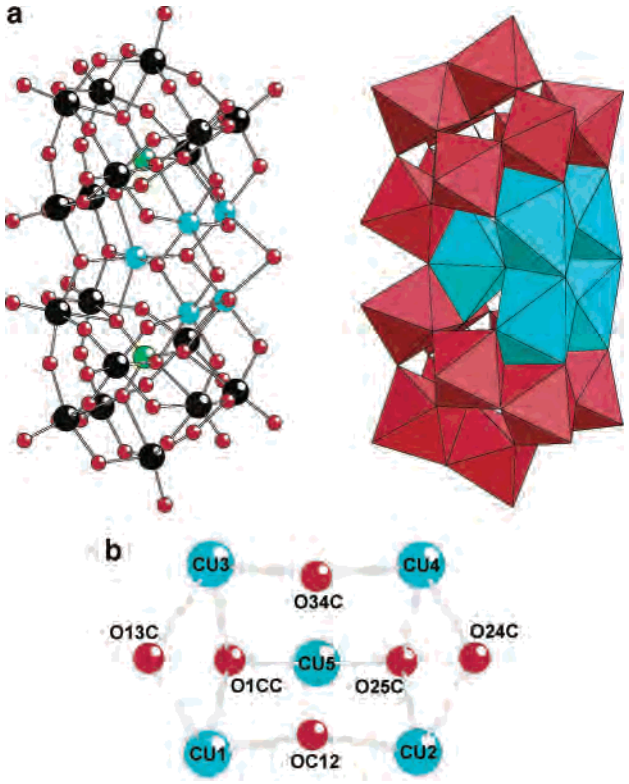

Figure 1. (a) Ball-and-stick (left) and polyhedral (right) representations of **1**. The color code is as follows: copper, turquoise; tungsten, black; silicon, green; oxygen, red. (b) Ball-and-stick representation of the central $\{Cu_5(OH)_4(H_2O)_2\}^{6+}$ fragment of **1**.

structural details of this $\{Cu_5(OH)_4(H_2O)_2\}^{6+}$ fragment are of interest (see Figure 1b). Bond valence sum calculations indicate that all bridging oxo groups linking adjacent copper atoms are either mono- or diprotonated.[24] Specifically, oxygen atoms O1CC, OC12, O25C, and O34C are monoprotonated (OH), whereas oxygen atoms O13C and O24C are diprotonated (H_2O).

As expected, the octahedral coordination spheres of all copper(II) centers are Jahn−Teller distorted. The equatorial Cu−O distances range from 1.907 to 2.084(13) Å, whereas the axial Cu−O distances are 2.280 to 2.387(13) Å. The Cu−O−Cu angles of the central $\{Cu_5(OH)_4(H_2O)_2\}^{6+}$ fragment range from 83.6 to 129.3(6)°, and the Cu···Cu separations in **1** range from 3.11 to 3.56 Å.

The novel pentacopper-substituted polyanion **1** is highly interesting for magnetic, EPR, electrochemical, electrocatalysis, and MS studies.

Magnetochemistry. Figure 2a shows magnetic susceptibility data for **K-1** as a plot of $\chi_m T$ vs T, where T is the temperature in Kelvin. $\chi_m T$ steadily decreases upon cooling from 1.15 emu·K/mol at 300 K to 0.44 emu·K/mol at 80 K and slowly saturates to 0.39 emu·K/mol as the temperature further decreases to 1.8 K. Comparison of the low-temperature saturation value (0.39 emu·K/mol) to the calculated value of 0.41 emu·K/mol for $S = {}^1/_2$ and $g = 2.1$ implies $S_T = {}^1/_2$ as the spin of the ground state.

(19) (a) Vulfson, S. G. *Molecular Magnetochemistry*; Gordon and Breach Science: Newark, NJ, 1998. (b) Kahn, O. *Molecular Magnetism*; VCH: New York, 1993.
(20) (a) Cage, B.; Hassan, A. K.; Pardi, L. A.; Krzystek, J.; Brunel, L.-C.; Dalal, N. S. *J. Magn. Reson.* **1997**, *124*, 495. (b) Hassan, A. K.; Pardi, L. A.; Krzystek, J.; Sienkiewicz, A.; Goy, P.; Rohrer, M.; Brunel, L.-C. *J. Magn. Reson.* **2000**, *142*, 300.
(21) Keita, B.; Girard, F.; Nadjo, L.; Contant, R.; Canny, J.; Richet, M. *J. Electroanal. Chem.* **1999**, *478*, 76.
(22) Håkansson, K.; Chalmers, M. J.; Quinn, J. P.; McFarland, M. A.; Hendrickson, C. L.; Marshall, A. G. *Anal. Chem.* **2003**, *75*, 3256.
(23) Laronze, N.; Marrot, J.; Hervé, G. *Chem. Commun.* **2003**, 2360.
(24) Brown, I. D.; Altermatt, D. *Acta Crystallogr.* **1985**, *B41*, 244.

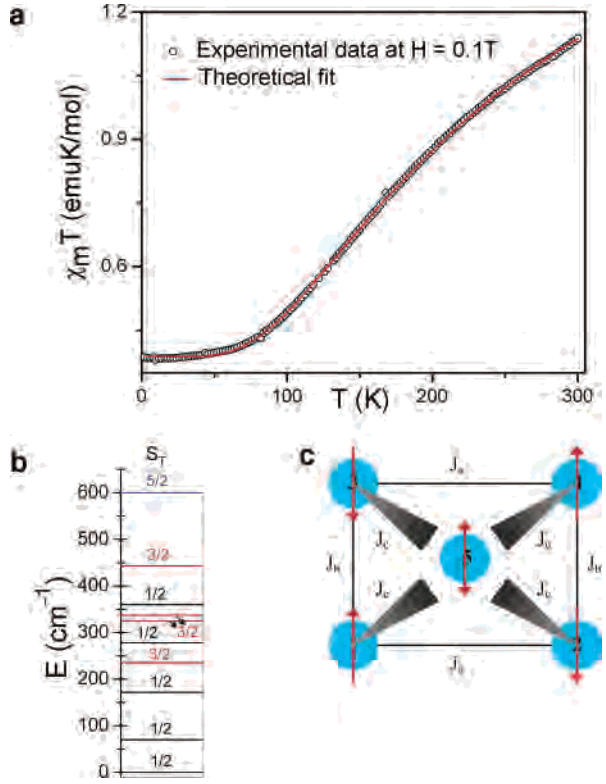

Figure 2. (a) Plot of $\chi_m T$ vs T for **K-1** at $H = 0.1$ T. (b) Calculated spin-state energies, relative to the ground state of **K-1**. The color code is as follows: $S_T = {}^1/_2$ (black), $S_T = {}^3/_2$ (red), and $S_T = {}^5/_2$ (blue). (c) Spin-exchange coupling in the $\{Cu_5(OH)_4(H_2O)_2\}^{6+}$ core of **K-1**, where the numbering corresponds to that of Figure 1b. Up and down arrows on the apical Cu^{II} ion (Cu5) represent the spin frustration experienced by it.

Following the numbering scheme in Figure 1b, the isotropic spin-exchange Hamiltonian for **1** can be given as

$$\hat{H}_{exch} = -2[J_{12}\hat{S}_1\cdot\hat{S}_2 + J_{24}\hat{S}_2\cdot\hat{S}_4 + J_{34}\hat{S}_3\cdot\hat{S}_4 + J_{13}\hat{S}_1\cdot\hat{S}_3 + J_{15}\hat{S}_1\cdot\hat{S}_5 + J_{25}\hat{S}_2\cdot\hat{S}_5 + J_{45}\hat{S}_4\cdot\hat{S}_5 + J_{35}\hat{S}_3\cdot\hat{S}_5] \quad (1)$$

Considering the C_{2v} symmetry of the pentamer, the above Hamiltonian can be rewritten as

$$\hat{H}_{exch} = -2J_a[\hat{S}_1\cdot\hat{S}_2 + \hat{S}_3\cdot\hat{S}_4] - 2J_b[\hat{S}_1\cdot\hat{S}_3 + \hat{S}_2\cdot\hat{S}_4] - 2J_c[\hat{S}_1\cdot\hat{S}_5 + \hat{S}_2\cdot\hat{S}_5 + \hat{S}_4\cdot\hat{S}_5 + \hat{S}_3\cdot\hat{S}_5] \quad (2)$$

where $J_{12} = J_{34} = J_a$, $J_{13} = J_{24} = J_b$, and $J_{15} = J_{25} = J_{35} = J_{45} = J_c$. The Hamiltonian in eq 2 gives rise to 10 spin states corresponding to the total spin operator $\hat{S}_T = \hat{S}_1 + \hat{S}_2 + \hat{S}_3 + \hat{S}_4 + \hat{S}_5$, viz., five doublets ($S_T = {}^1/_2$), four quartets ($S_T = {}^3/_2$), and one sextet ($S_T = {}^5/_2$). The eigenvalues associated with the Hamiltonian in eq 2, obtained by solving the 32×32 matrix (see the Appendix for details), are listed in Table 2. The molar magnetic susceptibility expression shown in eq 3 was then obtained by substituting the energies given in Table 2 in the Heisenberg−Dirac−van Vleck equation.[19b]

$$\chi_m = \left(\frac{Ng^2\beta^2}{4kT}\right)\left(\frac{A}{B}\right) \quad (3)$$

Here N is Avogadro's number, g is the Landé g factor, β is the electron Bohr magneton, k is the Boltzmann constant, T is the temperature in Kelvin, $A = 35\exp(2x + 2y + 5z) + 10\exp(2y + 4z) + 10\exp(2x + 4z) + 10\exp(4z) + 10\exp(2x + 2y) + \exp(3z + 2\sqrt{x^2-xy+y^2}) + \exp(3z - 2\sqrt{x^2-xy+y^2}) + \exp(2y + z) + \exp(2x + z) + \exp(z)$, and $B = 3\exp(2x + 2y + 5z) + 2\exp(2y + 4z) + 2\exp(2x + 4z) + 2\exp(4z) + 2\exp(2x + 2y) + \exp(3z + 2\sqrt{x^2-xy+y^2}) + \exp(3z - 2\sqrt{x^2-xy+y^2}) + \exp(2y + z) + \exp(2x + z) + \exp(z)$, with $x = J_a/kT$, $y = J_b/kT$, and $z = J_c/kT$.

The experimental data were fitted to eq 3 with g, J_a, J_b, and J_c as fitting parameters. As shown in Figure 2a, the least-squares fit is quite satisfactory and yields $J_a = -51 \pm 6$ cm^{-1}, $J_b = -104 \pm 1$ cm^{-1}, $J_c = -55 \pm 3$ cm^{-1}, and $g = 2.035 \pm 0.002$. The spin-state spectrum along with the energies relative to the ground state is shown in Figure 2b. The doublet ground state is well separated from the first excited state ($S_T = {}^1/_2$) by ~70 cm^{-1} (~101 K), which is consistent with our EPR results (vide infra).

The observed J values can be correlated with the molecular structure by considering the available exchange pathways between the Cu^{2+} ions (see Table 3 for bond lengths and angles). Cu1(3)···Cu2(4) are connected via a μ_2-OH with a bridging angle of about 129°, and Cu1(2,3,4)···Cu5 are connected via a μ_3-OH with a bridging angle of about 123°, thus giving rise to antiferromagnetic exchange interactions ($J_a = -51 \pm 6$ cm^{-1} and $J_c = -55 \pm 3$ cm^{-1}, respectively). On the other hand, Cu1(2)···Cu3(4) are connected via both a μ_2-OH_2 and a μ_3-OH with bridging angles of about 84° and 100°, respectively, and therefore can interact either ferromagnetically or antiferromagnetically.[25] Considering that the Cu−O bond lengths (~2.05 Å) are shorter along the μ_3-OH bridge than the μ_2-OH_2 (~2.33 Å) and the fact that Cu1-

Table 2. Eigenvalues Associated with the Spin-Exchange Hamiltonian for **1**[a]

n	S_T	$E(S_T)$
1	${}^5/_2$	$-J_a - J_b - 2J_c$
2	${}^3/_2$	$J_a - J_b - J_c$
3	${}^3/_2$	$-J_a + J_b - J_c$
4	${}^3/_2$	$J_a + J_b - J_c$
5	${}^3/_2$	$-J_a - J_a + 3J_c$
6	${}^1/_2$	$J_a + J_b - 2\sqrt{J_a^2 - J_aJ_b + J_b^2}$
7	${}^1/_2$	$J_a + J_b + 2\sqrt{J_a^2 - J_aJ_b + J_b^2}$
8	${}^1/_2$	$J_a - J_b + 2J_c$
9	${}^1/_2$	$-J_a + J_b + 2J_c$
10	${}^1/_2$	$J_a + J_b + 2J_c$

[a] See text for details.

Table 3. Bond Distances (Å) and Angles (deg) for the Central $\{Cu_5(OH)_4(H_2O)_2\}^{6+}$ Fragment in **1**

	Cu1	Cu2	Cu3	Cu4	Cu5	Cu−O−Cu
O13C	2.28(1)		2.37(1)			85.0(5)
OC12	1.95(1)	1.92(1)				128.4(6)
O24C		2.30(2)		2.37(2)		83.6(5)
O34C			1.95(1)	1.91(1)		129.3(7)
O1CC	2.09(1)		2.02(1)		1.96(1)	100.2(5), 122.6(6), 123.1(6)
O25C		2.05(1)		2.03(1)	1.98(1)	99.5(5), 122.8(6), 123.1(6)

(25) (a) Crawford, V. H.; Richardson, H. W.; Wasson, J. R.; Hodgson, D. J.; Hatfield, W. E. *Inorg. Chem.* **1976**, *15*, 2107. (b) Buvaylo, E. A.; Kokozay, V. N.; Vassilyeva, O. Y.; Skelton, B. W.; Jezierska, J.; Brunel, L.-C.; Ozarowski, A. *Inorg. Chem.* **2005**, *44*, 206.

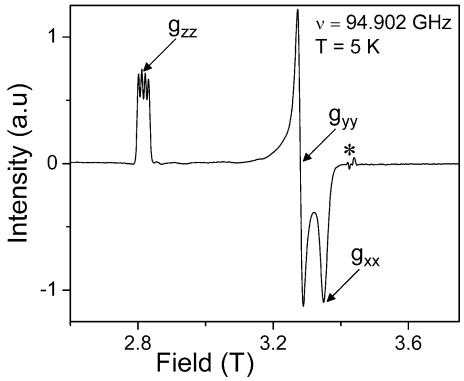

Figure 3. Polycrystalline powder EPR spectrum of **K-1** at 94.902 GHz and 5 K. The asterisk in the figure is from an impurity. See text for details.

(2,3,4)····Cu5 interact antiferromagnetically via the same μ_3-OH bridge, we believe that Cu1(2)····Cu3(4) are antiferromagnetically coupled via the μ_3-OH bridge ($J_b = -104 \pm 1$ cm^{-1}). The magnetic exchange parameters obtained in the present study are consistent with other pentanuclear Cu^{2+} complexes reported in the literature.[26] The spin-exchange coupling scheme is shown in Figure 2c, where Cu1, Cu2, Cu3, and Cu4 are in the plane of paper and Cu5 is projecting out of the plane. The dominant antiferromagnetic exchange interactions in the plane align the spins antiparallel, thus making Cu5 a spin-frustrated center.

EPR. Q-band (34 GHz) as well as 95- and 190-GHz EPR measurements were carried out to complement our magnetic susceptibility measurements. Figure 3 shows a 95-GHz powder spectrum of **K-1** at 5 K, and it is a typical Cu^{2+} spectrum, with a four-line hyperfine structure (A_{zz}) on the low-field Zeeman peak (g_{zz}). We assign it to the spin-frustrated apical Cu^{2+} ion. A_{xx} and A_{yy} were not resolved, implying that their magnitude is at least $^1/_3$ of the observed line widths. The small high-field peaks marked with an asterisk are from impurities. As the temperature increases, the hyperfine structure broadens out and disappears at about 45 K, and finally the overall spectrum also broadens and becomes unobservable above 60 K (see Figure 4). Neither the g values nor the A_{zz} values exhibited any temperature dependence in the range investigated, implying that the observed spectrum originates from a ground state, here $S_T = {}^1/_2$ as discussed above. Figure 5 shows a representative simulation at 95 GHz and 5 K. The agreement between the observed and simulated spectra is considered to be satisfactory. The fact that the spectra at all frequencies were reproduced satisfactorily with the Hamiltonian parameters $g_{zz} = 2.4073 \pm 0.0005$, $g_{yy} = 2.0672 \pm 0.0005$, $g_{xx} = 2.0240 \pm 0.0005$, and $|A_{zz}| = 340 \pm 20$ MHz (0.0113 cm^{-1}) implies that there is no net exchange field. We assigned a negative sign for A_{zz} based on the literature,[27] i.e., $A_{zz} = -340 \pm 20$ MHz (-0.0113 cm^{-1}), as expected from the 3d → inner s

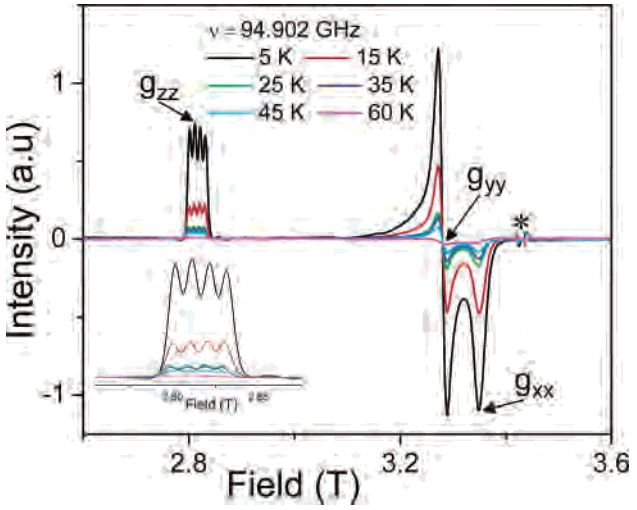

Figure 4. Temperature dependence of powder EPR spectra of **K-1** at 94.902 GHz. The inset shows the magnified low-field Zeeman peak. The asterisk in the figure is from an impurity. See text for details.

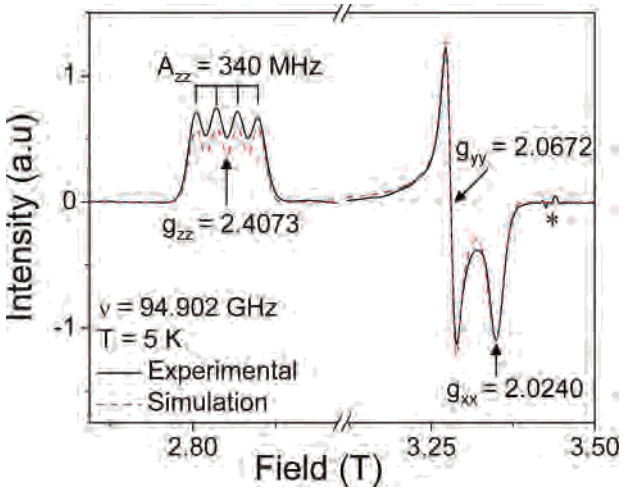

Figure 5. Experimental and simulated powder EPR spectra of **K-1** at 94.902 GHz and 5 K. The experimental spectrum was simulated by a Gaussian line shape with line widths $B_{xx} = 23 \pm 2$ mT, $B_{yy} = 13 \pm 2$ mT, and $B_{zz} = 7 \pm 0.5$ mT.

electron-spin-polarization mechanism. The observed g anisotropy is not surprising if we consider the elongated rhombic-octahedral stereochemistry around Cu5 of **1** (see Figure 6). The g and A values observed for our copper pentamer are consistent with the literature values reported[27,28] for a single octahedral oxygen-coordinated Cu^{2+} ion with rhombic distortion and imply that the unpaired electron resides in a $3d_{x^2-y^2}$ type of molecular orbital. Below, we discuss the relationship between these parameters and the nature of the chemical bonding around the apical Cu^{2+} ion (Cu5 center) in terms of a simple molecular orbital−crystal field model.

(26) (a) Gojon, E.; Gaillard, J.; Latour, J.-M.; Laugier, J. *Inorg. Chem.* **1987**, *26*, 2046. (b) Shanmugam, M.; Muthuvijayan, L.; Tiwary, S. K.; Chakravarty, A. R. *Inorg. Chem.* **1995**, *34*, 5091. (c) Doyle, A. A.; Parsons, S.; Solan, G. A.; Winpenny, E. P. *J. Chem. Soc., Dalton Trans.* **1997**, 2131. (d) Song, Y.; Liu, J.-C.; Liu, Y.-J.; Zhu, D.-R.; Zhuang, J.-Z.; You, X.-Z. *Inorg. Chim. Acta* **2000**, *305*, 135. (e) Papaefstathiou, G. S.; Raptopoulou, C. P.; Tsoshos, A.; Terzis, A.; Bakalbassis, E. G.; Perlepes, S. P. *Inorg. Chem.* **2000**, *39*, 4658.

(27) (a) Maki, A. H.; McGarvey, B. R. *J. Chem. Phys.* **1958**, *29*, 31 and 35. (b) McGarvey, B. R. *J. Phys. Chem.* **1967**, *71*, 51.

(28) For example, see: (a) Hathaway, B. J.; Billing, D. E. *Coord. Chem. Rev.* **1970**, *5*, 143. (b) Abragam, A.; Bleaney, B. *Electron Paramagnetic Resonance of Transition Ions*; Dover Publications: New York, 1970. (c) Pilbrow, J. R. *Transition Ion Electron Paramagnetic Resonance*; Oxford University Press: New York, 1990. (d) Dalal, N. S.; Millar, J. M.; Jagadeesh, M. S.; Seehra, M. S. *J. Chem. Phys.* **1981**, *74*, 1916.

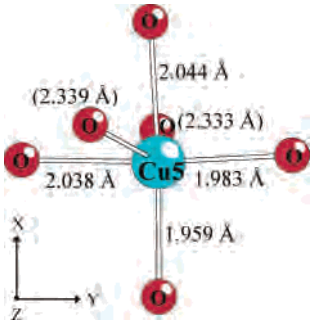

Figure 6. Coordination environment of Cu5 in **K-1**. The bond lengths are given in order to show the distortion present at the Cu center. The choice of *x* and *y* axes is arbitrary.

Considering that the apical Cu^{2+} ion is in an all-oxygen ligand environment, the small differences in Cu5−O_{eq} bond lengths will be ignored and the site symmetry of Cu^{2+} will be taken as C_{4v}. Unfortunately, our lack of resolution regarding the measurement of A_{xx} and A_{yy} and the approximation of C_{4v} site symmetry for the apical Cu^{2+} ion render the following discussion to be only qualitative, but nevertheless instructive. Furthermore, we shall use the expressions[27,28a,c,29] reported for a D_{4h} Cu^{2+} ion with $3d_{x^2-y^2}$ ground state. This assumption is justified because Hathaway and Billing have shown[28a] that the expressions for the *g* values are the same for equivalent point groups, provided the ground state is identical. In other words, *g*-value expressions for D_4, D_{4h}, C_{4v}, and D_{2d} symmetries will be the same if the ground state of a metal ion is identical in all of the point groups.

On the basis of group theory, allowance for covalent bonding is made by combining the proper linear combination of ligand orbitals with the copper d orbitals to give the wave functions of the form[27,28a,c,d,29]

$$\psi_{B1}(x^2-y^2) = \alpha d_{x^2-y^2} + (1-\alpha^2)^{1/2}\psi_{B1}(\text{oxygen})$$

$$\psi_{A1}(3z^2-r^2) = \beta d_{3z^2-r^2} + (1-\beta^2)^{1/2}\psi_{A1}(\text{oxygen})$$

$$\psi_{B2}(xy) = \gamma d_{xy} + (1-\gamma^2)^{1/2}\psi_{B2}(\text{oxygen})$$

$$\psi_{E}(xz,yz) = \delta d_{xz,yz} + (1-\delta^2)^{1/2}\psi_{E}(\text{oxygen}) \quad (4)$$

When these wave functions are applied to the Hamiltonian of Abragam and Pryce[28b,30] (cf. eq 5), the magnetic parameters obtained[27,28a,c,d,29] are given in eq 6.

$$\hat{H} = g_{||}\beta H_z\hat{S}_z + g_{\perp}\beta(H_x\hat{S}_x + H_y\hat{S}_y) + A_{||}S_z\hat{I}_z + A_{\perp}(S_x\hat{I}_x + S_y\hat{I}_y) \quad (5)$$

$$g_{||} = 2.0023 - 8\lambda\alpha^2\gamma^2/\Delta E_{xy} \quad (6a)$$

$$g_{\perp} = 2.0023 - 2\lambda\alpha^2\delta^2/\Delta E_{xz,yz} \quad (6b)$$

$$A_{||} = P[-\kappa - (4/7)\alpha^2 + (g_{||} - 2.0023) + (g_{\perp} - 2.0023)] \quad (6c)$$

$$A_{\perp} = P[-\kappa + (2/7)\alpha^2 + (11/14)(g_{\perp} - 2.0023)] \quad (6d)$$

In the expressions 6a−d, λ is the spin−orbit coupling constant for a free ion, $\Delta E_{xy} = E_{xy} - E_{x^2-y^2}$, $\Delta E_{xz,yz} = E_{xz,yz} - E_{x^2-y^2}$, $P = 2.0023 g_n\beta_e\beta_n\langle r^{-3}\rangle_{av}$, and κ is the isotropic hyperfine (contact) term arising from the polarization of inner s electrons by the unpaired spin in the d orbital.

The values for ΔE_{xy} and $\Delta E_{xz,yz}$ were determined by running the optical absorption of **K-1** in an aqueous solution. The spectrum consists of a broad peak around 1.2×10^4 cm^{-1} and, on the basis of the literature,[28a,31] is taken as ΔE_{xy}. The intense charge-transfer transitions set in at $\sim 2.5 \times 10^4$ cm^{-1} with no hint of any shoulder. We therefore take $\Delta E_{xz,yz} \geq 2.5 \times 10^4$ cm^{-1}. On the basis of $\lambda = -828$ cm^{-1} (free-ion value for Cu^{2+}), $P = 0.036$ cm^{-1} (free-ion value for Cu^{2+}), $\kappa = 0.33$, $g_{||} = g_{zz} = 2.4073$, $g_{\perp} = (g_{xx} + g_{yy})/2 = 2.0456$, and $A_{||} = A_{zz} = -0.0113$ cm^{-1} in eqs 6a−c, the following values can be deduced for the bonding parameters α, γ, and δ:

$$\alpha^2 = 0.71, \quad \gamma^2 = 1.0, \quad \delta^2 \geq 0.92$$

These values are in reasonable agreement with other similar tetragonal Cu^{2+} complexes reported in the literature.[27,28a,c,29] A value of 0.71 for α^2 indicates a moderate ($\sim$30%) contribution from the oxygen orbitals.

Electrochemistry. The cyclic voltammogram (CV) of **1** in a pH 5 medium is shown in Figure 7A. In the potential domain explored, it consists of four reduction waves with peak potentials located respectively at −0.170, −0.268, −0.736, and −0.858 V vs SCE. The last two chemically reversible waves are attributed to the redox processes of the W centers. To the first two reduction waves is associated a single oxidation process located at +0.056 V, with the characteristic shape usually encountered for by the oxidation of adsorbed species. These first two waves and their oxidation counterpart are attributed to the redox processes of the Cu^{2+} centers. The shapes and potential locations of the CV of **1** are comparable to those observed for the CV of $CuSO_4$ under the same concentration and supporting electrolyte conditions.[32] The reduction peak potentials of $CuSO_4$ are located at −0.156 and −0.442 V, respectively. In both compounds, the pattern features the two-step reduction of Cu^{2+} to Cu^0 through Cu^{1+}, generally observed in the presence of strong ligands such as Cl^- or NH_3.[33−35] Figure 7B

(29) (a) Stevens, K. W. H. *Proc. R. Soc. London* **1953**, *A219*, 542. (b) Owen, J. *Proc. R. Soc. London* **1955**, *A227*, 183; *Discuss. Faraday Soc.* **1955**, *19*, 127. (c) Kivelson, D.; Neiman, R. *J. Chem. Phys.* **1961**, *35*, 149. (d) Gersmann, H. R.; Swalen, J. D. *J. Chem. Phys.* **1962**, *36*, 3221.
(30) Abragam, A.; Pryce, H. M. L. *Proc. R. Soc. London* **1951**, *A205*, 135; **1951**, *A206*, 164.
(31) Billing, D. E.; Hathaway, B. J. *J. Chem. Soc. A* **1968**, 1516.
(32) Keita, B.; Mbomekalle, I. M.; Nadjo, L. *Electrochem. Commun.* **2003**, *5*, 830.
(33) Greenwood, N. N.; Earnshaw, A. *Chemistry of the Elements*, 2nd ed.; Butterworth-Heinemann: Oxford, U.K., 1997; pp 1193−2000.
(34) Walcarius, A.; Despas, C.; Bessières, J. *Anal. Chim. Acta* **1999**, *385*, 79.
(35) Keita, B.; Abdeljalil, E.; Nadjo, L.; Avisse, B.; Contant, R.; Canny, J.; Richet, M. *Electrochem. Commun.* **2000**, *2*, 145.

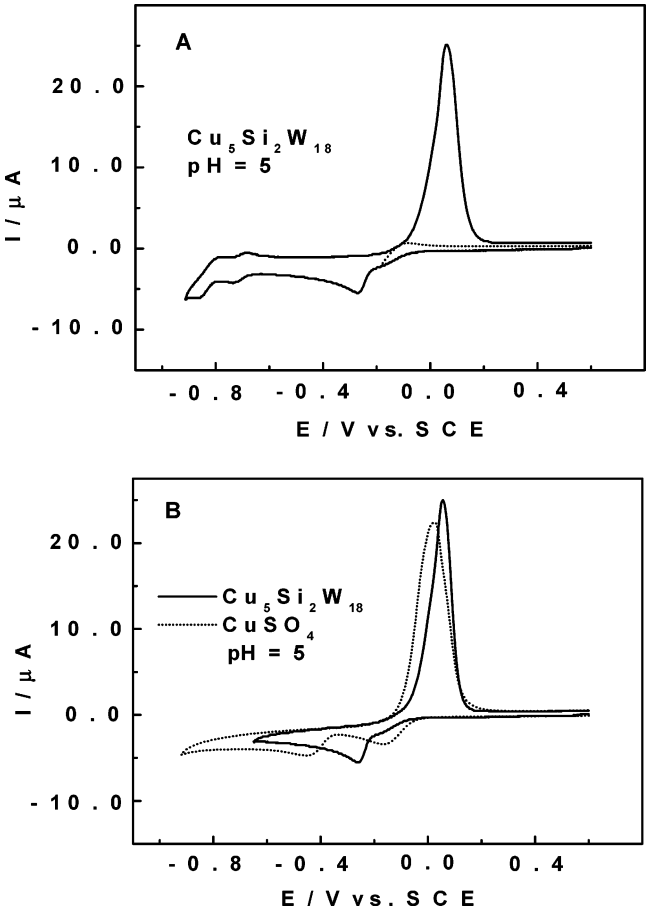

Figure 7. CVs run in a pH 5 (0.4 M $CH_3COONa + CH_3COOH$) buffer solution. The scan rate was 10 mV/s, the working electrode was GC, and the reference electrode was SCE. For more detailed information, see the text. (A) CV of 2×10^{-4} M **1** restricted to the Cu waves and the first two W waves. (B) Superposition of the CV of 2×10^{-4} M **1** restricted to the Cu waves with the CV of 2×10^{-4} M $CuSO_4$. This last CV was multiplied by 4 for an easier comparison.

compares their CVs and indicates that these two steps are better separated for $CuSO_4$ than **1**.[36] Controlled potential coulometry just negative of the peak potential of the second reduction process of **1** indicates the consumption of 10.05 $\pm$ 0.05 electrons per molecule, indicating that the five Cu^{2+} centers are actually reduced.

Like the observations made for most POMs, the electrochemical characteristics of **1** are pH-dependent. Figure 8 illustrates such variations for Cu and W waves of **1** when the pH varies from 5 to 3. The expected classical positive potential shift of the whole CV pattern was obtained when the acidity of the supporting electrolyte increased. The Cu waves are practically merged in the pH 3 medium, and the charge released by the reoxidation of the corresponding deposited Cu^0 was roughly 20% larger than that measured in the pH 5 medium. In another respect, the Cu^0 deposition occurs more easily from the pH 3 medium and was found

(36) Actually, comparison of the CVs of 0.2 and 0.5 mM $CuSO_4$ reveals that the exact potential location of the second reduction wave of the salt depends on its initial concentration and shifts in the positive direction when the concentration increases. This observation can be understood by considering that the second reduction of Cu^{2+} occurs on larger and larger amounts of deposited Cu^0 when the concentration of $CuSO_4$ increases.

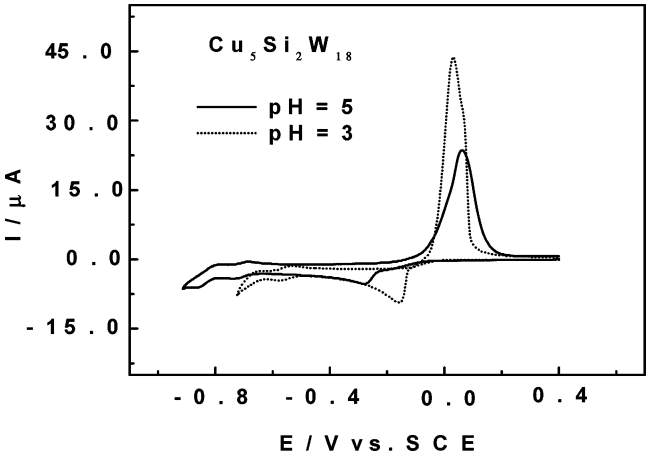

Figure 8. Comparison of the CVs of 2×10^{-4} M **1** restricted to the Cu waves in pH 3 (0.2 M $Na_2SO_4 + H_2SO_4$) and pH 5 (0.4 M $CH_3COONa + CH_3COOH$) media. The scan rate was 10 mV/s, the working electrode was GC, and the reference electrode was SCE.

to start readily from the very beginning of the composite Cu^{2+} wave. Analogous observations were made with Cu sandwich-type POMs, $[Cu_4(H_2O)_2(X_2W_{15}O_{56})_2]^{16-}$ (X = As or P) (abbreviated as $\mathbf{Cu_4X_4W_{30}}$).[32]

Among the explanations that might be offered for this observation, the following could be retained: (i) the complexing ability of the POM framework is depressed when its overall negative charge is decreased upon protonation; (ii) the SO_4^{2-} anions present in the pH 3 medium are less powerful stabilizing agents than CH_3COO^- anions for the Cu^+ species. In a continuation of this reasoning, it was interesting to study the competition between the POM framework and chloride anions for the complexation of the copper centers in the pH 3 sulfate medium, where the reduced Cu^+ forms might experience a weak stabilization by the oxometalate. For example, upon addition of a 500-fold excess of chloride (0.1 M Cl^- vs 0.2 mM of **1**), a partial extraction of Cu^{2+} from the POM was observed and the extracted Cu^{2+} showed the same CV as $CuSO_4$.[32] These results indicate that, in such special conditions, the copper sandwich-type compounds ($\mathbf{Cu_4X_4W_{30}}$, X = As or P) are more stable against copper extraction. As a matter of fact, despite a slight modification of their CVs attributed to the replacement of H_2O ligands by chloride, no extraction of Cu^{2+} was obtained even with 1 M Cl^- (5000-fold excess).[32] Finally, the W waves are clearly separated from the Cu waves. Note that, in the pH 3 medium, the second W wave is very close to an irreversible wave with a large current (Figure S1 in the Supporting Information). As for Cu-monosubstituted POMs,[21] this wave, located at -0.875 V, is attributed to the hydrogen evolution reaction on Cu^0 deposited on the GC electrode.

Electrocatalysis of NO_x Reduction. Nitrate reduction was selected to test the catalytic abilities of **1**. Studies of NO_2^- and N_2O, which are possible intermediate chemicals in the reduction of nitrate, were also carried out. In the following, all electrocatalysis tests were performed in a pH 5 medium.

(a) Reduction of Nitrate. The CVs were run as a function of the excess parameter γ ($\gamma = C_{NO_3^-}/C_{POM}$) with the same

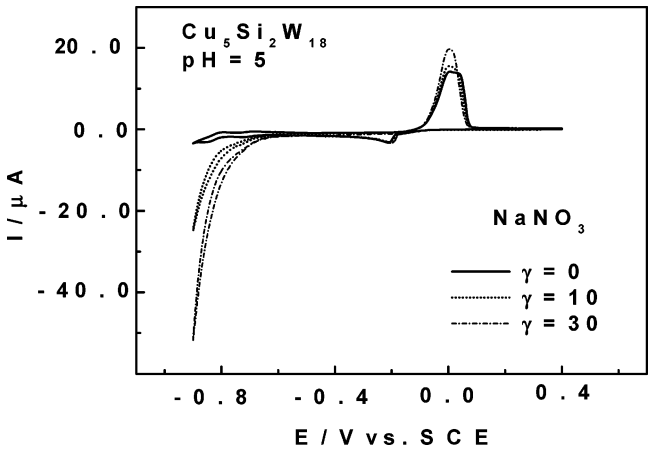

Figure 9. Electrocatalysis of the reduction of nitrate in the presence of 2×10^{-4} M **1** in a pH 5 medium (0.4 M $CH_3COONa + CH_3COOH$). The scan rate was 2 mV/s, the working electrode was GC, and the reference electrode was SCE.

potential scan rate. As is apparent from Figure 9, the addition of even modest amounts of nitrate induced a large cathodic current enhancement, starting in a potential domain of the first W wave. Concomitantly, the reversibility of the W waves was suppressed. These observations indicate an efficient reduction of nitrate by the reduced species of **1**. In the explored potential domain, no reduction of nitrate could be obtained on the GC electrode in the absence of POM.[37] The current increase can be expressed more quantitatively through the catalytic efficiency CAT defined as

$$\mathrm{CAT} = 100(I_{\mathrm{POM}+\mathrm{NO_3^-}} - I^{\mathrm{d}}_{\mathrm{POM}})/I^{\mathrm{d}}_{\mathrm{POM}}$$

where $I_{\mathrm{POM}+\mathrm{NO_3^-}}$ represents the reduction current of the POM in the presence of nitrate and $I^{\mathrm{d}}_{\mathrm{POM}}$ the reduction current for the POM alone. In the present experiments, CAT values, measured at -0.9 V, varied from 618% to 1393% for $\gamma =$ 10 and 30, respectively. Corresponding CAT values evaluated in the same conditions as those for copper sandwich-type POMs (**$Cu_4X_4W_{30}$**, X = As or P)[32] were distinctly lower than those obtained here. The results for such CAT values are gathered for comparison in the Supporting Information (see Table S1). For example, the CAT value measured at -0.9 V and $\gamma = 30$ for **$Cu_4P_4W_{30}$** was roughly 4 times smaller than that for **1**, as seen in this table.[38]

(b) Reduction of NO_2^- and N_2O. Figure 10A indicates that, upon reduction, **1** catalyzes also the reduction of nitrite at pH 5. This reduction was found to occur before the deposition of a substantial amount of Cu^0, in a potential domain distinctly positive of that necessary for nitrate reduction. The CAT values for **1** and **$Cu_4X_4W_{30}$** (X = As or P) were less different than observed in the case of nitrate.

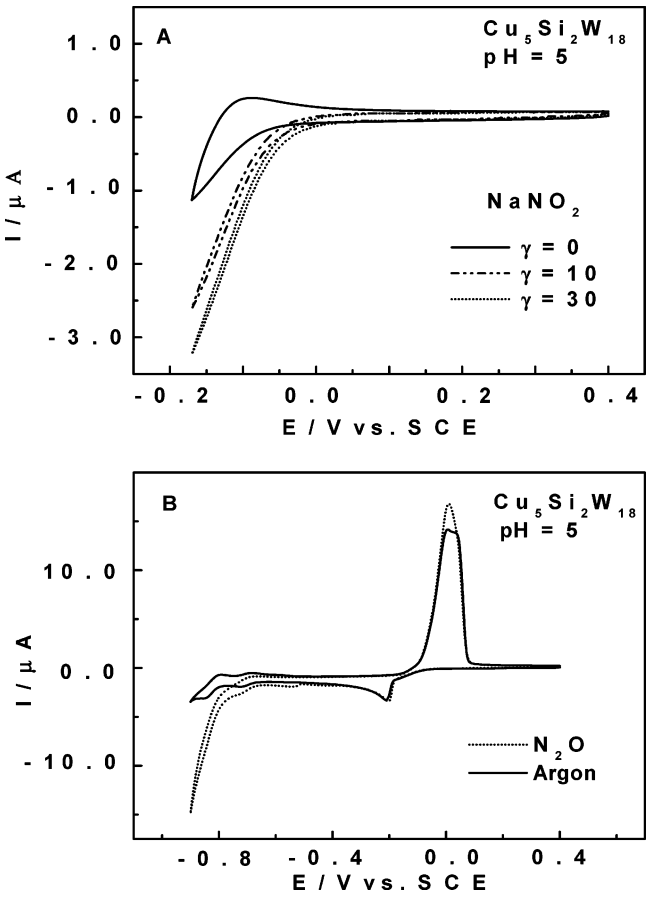

Figure 10. Electrocatalysis of the reduction of two NO_x in the presence of 2×10^{-4} M **1** in a pH 5 medium (0.4 M $CH_3COONa + CH_3COOH$). The scan rate was 2 mV/s, the working electrode was GC, and the reference electrode was SCE.

For example, the CAT value measured at -0.17 V and $\gamma =$ 30 was just 1.5 times larger for **1** than for **$Cu_4P_4W_{30}$**, compared to the 4-fold increase for nitrate. Tentatively, one possible explanation is that the reduction mechanisms of nitrite and nitrate are not the same. Provisionally, it must also be noted that **1** is a good electrocatalyst for nitrite reduction in more acidic media, where a mixture of NO and HNO_2 is present.[39] For example, Figure S2 (see the Supporting Information) compares the results obtained at pH 5 and 3. It was also found that **1** catalyzes the reduction of N_2O (see Figure 10B). To our knowledge, this is the first time that such a catalysis by a POM is described.

Finally, it emerges from the results of the electrocatalytic reduction of NO_x that Cu^{2+} ions complexed by POMs keep their catalytic properties with supplementary advantages. These advantages include the effect of accumulation of active Cu centers within **1**, a complex stable in a large pH domain (pH 1−7),[16] and the possibility of generating highly reduced products, owing to the electrons available in reduced W domains.

(37) Keita, B.; Abdeljalil, E.; Nadjo, L.; Contant, R.; Belghiche, R. *Electrochem. Commun.* **2001**, *3*, 56.

(38) The presence of one more Cu atom in **1** compared to **$Cu_4X_4W_{30}$** (X = As or P), inducing a surface increase during Cu^0 deposition in the former case, might not be the only parameter to explain this difference in catalytic efficiency. The quality of the deposited Cu^0 film might also intervene. For example, it is well-known that the particle size and morphology are important factors for the catalytic efficiency.

(39) At pH 3, the actual active species should be HNO_2 and/or NO. As a matter of fact, the sequence $HNO_2 \leftrightarrows H^+ + NO_2^-$ ($pK_a = 3.3$ at 18 °C) is known, and HNO_2 disproportionates in a fairly acidic solution: $3HNO_2 \rightarrow HNO_3 + 2NO + H_2O$. The rate of this reaction is known to be low.

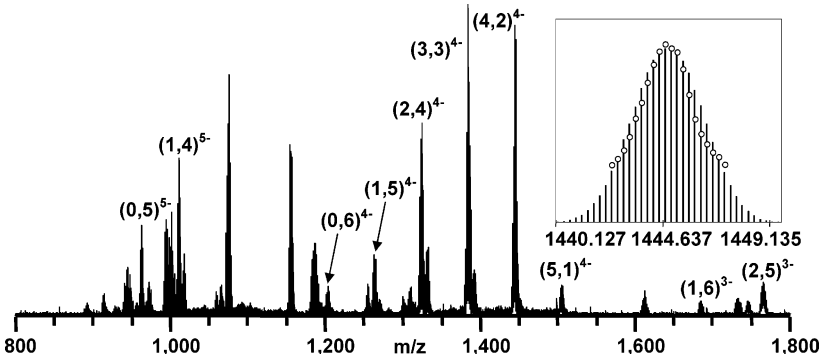

Figure 11. ESI FT-ICR negative-ion mass spectrum of $TBA_5H_5[Cu_5(OH)_4(H_2O)_2\ (SiW_9O_{33})_2]$ in acetonitrile. Labels denote the number of (TBA, H) counterions. All identified species feature a loss of two H_2O ligands from the Cu−hydroxo−aqua core. The inset shows the calculated (bars) and measured (circles) isotopic distributions for the $(4, 2)^{4-}$ species with the assigned formula $(TBA_4H_2[Cu^{II}_5(OH)_4(SiW_9O_{33})_2])^{4-}$.

Table 4. Accuracy of FT-ICR MS Measured Average *m*/*z* Values Relative to the Isotopic Distribution Computed for the Assigned Chemical Formula

	average *m*/*z*		
species	calcd from chemical formula	measd	error (ppm)
$(2, 5)^{3-}$	1765.76	1765.59	*a*
$(1, 6)^{3-}$	1685.30	1685.65	*a*
$(5, 1)^{4-}$	1505.11	1505.16	7
$(4, 2)^{4-}$	1444.76	1444.77	7
$(3, 3)^{4-}$	1384.41	1384.48	8
$(2, 4)^{4-}$	1324.07	1324.04	−9
$(1, 5)^{4-}$	1263.72	1263.79	10
$(0, 6)^{4-}$	1203.38	1203.39	10
$(1, 4)^{5-}$	1010.78	1010.80	13
$(0, 5)^{5-}$	962.50	962.43	−13

[a] The charge state is unambiguous, but the elemental composition cannot be determined with certainty because of a too low signal-to-noise ratio.

Mass Spectrometry. (a) Product Characterization by Electrospray Ionization (ESI) FT-ICR MS. Figure 11 shows the negative-ion mass spectrum of TBA_xH_{10-x}-$[Cu_5(OH)_4(H_2O)_2(SiW_9O_{33})_2]$ in acetonitrile. Consistent with the polyanionic nature of **1**, only negative ions were observed. The high resolution of FT-ICR MS allowed us to accurately assign a molecular formula to each species by comparing the MS data to putative isotopic distributions (see Figure 11, inset). The reported average *m*/*z* is the number-average *m*/*z* value for each isotopic distribution (Table 4). The precision (and thus accuracy) in the determination of *m*/*z* is proportional to the signal-to-noise ratio and digital resolution (data points per peak width).[40] Although many of the isotopic distributions exhibited relatively low S/N ratios and limited digital resolution, measurement accuracy, nevertheless, suffices for unequivocal assignment of chemical formulas.

The highest-magnitude peaks in the mass spectrum were assigned to a series of $\{TBA_xH_y[Cu_5(OH)_4(SiW_9O_{33})_2]\}^{n-}$ species. Series consisting of $n = 3-5$ species were observed. The assigned chemical formulas and overall charge values (determined from the reciprocal of the spacing between adjacent *m*/*z* peaks in a given isotopic distribution) of the MS species are consistent with 2+ and 6+ oxidation states of the Cu and W metal ions, respectively. This result is consistent with the charges obtained from X-ray diffraction (XRD) characterization of the K salt of **1** in the solid state. As previously reported for POM species in solution,[41] polyanion **1** exhibited a large degree of cationization, with the species differing in mass by 241.5 Da corresponding to the exchange of a TBA counterion for a proton. The exact ratio of TBA to H in the ion-exchanged product before dissolution is not known, but judging from the relative abundance of the species in the 4− charge envelope, polyanion **1** can accommodate three to four TBA counterions in solution, with the remaining charge balance carried out by protons. That observation is also in good agreement with steric considerations for TBA and **1**.

The loss of two H_2O molecules from the central Cu−hydroxo−aqua core was the only fragmentation observed in the MS data. The low affinity of these two H_2O molecules is consistent with their large Cu−O bond lengths [2.28−2.37(2) Å] based on the XRD structure.[16] It is not known if the two H_2O ligands are removed in solution through displacement by solvent molecules or in the ESI process by intermolecular collisions.

In addition to the Keggin dimer **1**, another species was observed by MS. That species behaves like a polyanion in that we observed a series of 2− and 3− species that differ by roughly 241.5 Da. The chemical formula for that species has not been assigned but is close in mass to a single Keggin structure. The presence of bound TBA counterions makes it unlikely that this species results from gas-phase dissociation of the Keggin dimer structure during ESI. As our infrared multiphoton dissociation (IRMPD) data show, the energy required for core splitting would have removed all of the bound TBA counterions.

(40) Chen, L.; Cottrell, C. E.; Marshall, A. G. *Chemom. Intell. Lab. Syst.* **1986**, *1*, 51.

(41) Bonchio, M.; Bortolini, O.; Conte, V.; Sartorel, A. *Eur. J. Inorg. Chem.* **2003**, 699.

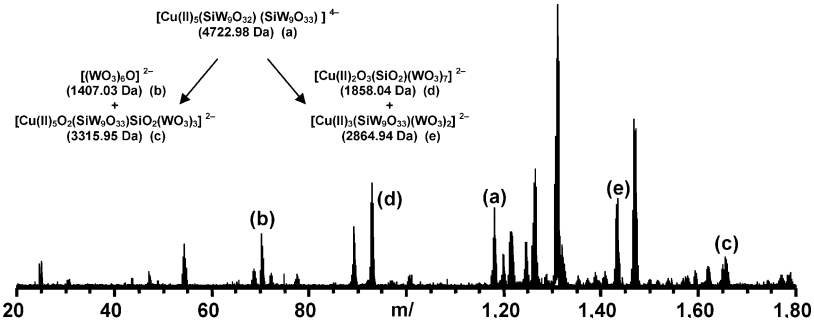

Figure 12. IRMPD FT-ICR MS/MS spectrum of quadrupole-isolated $TBA_4H_2[Cu_5(OH)_4(SiW_9O_{33})_2]$ precursor ions. Species a results from TBA and OH removal during the initial fragmentation. The subsequent appearance of fragments (b) + (c) and (d) + (e) is consistent with the fragmentation of a (see text for details).

(b) POM Fragmentation Analysis by IRMPD MS/MS. Fragmentation of Wells−Dawson-type POM derivatives (e.g., $[Nb_3P_2W_{15}O_{62}]^{9-}$) has previously been reported as part of the fast atom bombardment (FAB) MS characterization.[42,43] The observed fragmentation patterns provided important information regarding the structure of the parent ion and identities of stable fragments, worthy of investigation in their own right. Our fragmentation experiments differ from those above in that the soft ionization allowed us to separate MS and MS/MS experiments. Also, the use of IRMPD rather than collision-induced dissociation (CID) allowed more selective dissociation, with the dissociation of lowest-energy bonds taking place first.

The most abundant products from IRMPD of the isolated $\{TBA_2H_4[Cu_5(OH)_4(SiW_9O_{33})_2]\}^{4-}$ precursor at low (2.5 W/cm^2) laser irradiation intensity exhibit mass differences that correspond to the loss of TBAOH, H_2O, and OH^- fragments from the precursor. The lowest-mass species of significant abundance at average *m*/*z* 1180.8 was assigned to the formula $[Cu_5Si_2W_{18}O_{65}]^{4-}$, in which the Cu and W oxidation states were 2+ and 6+, respectively. That formula corresponds to a net loss of two TBAOH and three H_2O molecules from the parent ion. The most likely loss mechanism is the reaction of Cu−hydroxo core oxygen atoms with the TBA and H counterions. The higher basicity of those oxygen atoms relative to those in the Keggin unit makes them more likely to react with the counterions. Also, intermediate species consistent with the loss of oxygen atoms from intercalated metal−oxo fragments were observed after thermal decomposition of very large multi-Keggin-based POMs during conversion to tungsten bronzes.[44]

At higher irradiation intensity (5 W/cm^2), two sets of 2− fragments are observed such that the sums of the fragment masses and assigned formulas in each set yield the mass and formula of the $[Cu_5Si_2W_{18}O_{65}]^{4-}$ species (see Figure 12, inset). The two sets of fragments were assigned to the formulas $[W_6O_{19}]^{2-}$ and $[Cu_5Si_2W_{12}O_{46}]^{2-}$ and the formulas $[Cu_2SiW_7O_{26}]^{2-}$ and $[Cu_3SiW_{11}O_{39}]^{2-}$, respectively.

The first set of fragments has been observed previously during the fragmentation of Finke's $[Nb_3P_2W_{15}O_{62}]^{9-}$ during FAB MS, and both fragments have well-known solution analogues.[42] In particular, the fragment with the formula $[W_6O_{19}]^{2-}$ (corresponding to the well-known Lindqvist ion) was also previously observed during the formation of the Keggin structure in water[45] and as a CID fragment[46] of $[W_{10}O_{32}]^{4-}$. The absence of Cu in the $[W_6O_{19}]^{2-}$ fragment implies that removal of the oxygen atoms from the Cu−hydroxo core did not incorporate the Cu ions into the Keggin units.

The second fragmentation pathway is consistent with the separation of the two stable Keggin units along the former Cu_5−hydroxo core while keeping the two bridging tungsten atoms with the Cu_3-containing fragment. Because the ions in the second set are more abundant, it appears that this fragmentation pathway is more energetically favored than the first. The presence of a fragmentation mechanism not observed during FAB MS could be the result of a different structure of the parent ion or the differences between IRMPD and CID fragmentation. Further evidence of differences between the fragmentation methods is the presence of TBA counterions in the fragments observed by FAB. Finally, the apparent presence of multiple fragmentation pathways could also be explained by two precursor ions with one set of fragments quickly losing neutral species to give the appearance of a common precursor.

At the highest laser intensity (12 W/cm^2), a series of $(WO_3)_n$ structures similar to those previously reported for Wasfi's Wells−Dawson derivatives was observed.[43] The majority of the structures featured a Cu atom, further suggesting that the Cu forms strong bonds to the Keggin structure similar to the niobium in Finke's work.[42]

(42) (a) Finke, R. G.; Trovarelli, A. *Inorg. Chem.* **1993**, *32*, 6034. (b) Wasfi, S. H.; Costello, C. E. *Synth. React. Inorg. Met.−Org. Chem.* **1989**, *19*, 1059.
(43) Wasfi, S. H.; Costello, C. E.; Rheingold, A. L.; Haggerty, B. S. *Inorg. Chem.* **1991**, *30*, 1788.
(44) Wassermann, K.; Pope, M. T.; Salmen, M.; Dann, J. T.; Lunk, H. J. *J. Solid State Chem.* **2000**, *149*, 378.
(45) Deery, M. J.; Howarth, O. W.; Jennings, K. R. *J. Chem. Soc., Dalton Trans.* **1997**, 4783.
(46) Lau, T. C.; Wang, J.; Guevermont, R.; Siu, K. W. *J. Chem. Soc., Chem. Commun.* **1995**, 877.

Conclusions

Polyanion **1** has been characterized by several analytical techniques in the solid state (magnetism and EPR), in solution (electrochemistry and electrocatalysis), and in the gas phase (MS).

The magnetization and EPR studies establish that the $\{Cu_5(OH)_4(H_2O)_2\}^{6+}$ in **K-1** has a spin-doublet ($S_T = {}^1/_2$) ground state, with the unpaired electron localized mainly on the apical Cu^{2+} ion. The ground state is separated from the first excited $S_T = {}^1/_2$ spin state by $\sim$70 cm^{-1} ($\sim$101 K). EPR spectra were satisfactorily simulated with the spin Hamiltonian parameters $g_{zz} = 2.4073 \pm 0.0005$, $g_{yy} = 2.0672 \pm 0.0005$, $g_{xx} = 2.0240 \pm 0.0005$, and $A_{zz} = -340 \pm 20$ MHz (-0.0113 cm^{-1}). The g values are consistent with a $3d_{x^2-y^2}$-type molecular orbital ground state, as expected for a Cu^{2+} ion in an axially-elongated octahedral coordination with oxygen. A qualitative analysis of the g and A_{zz} values yields $\alpha^2 = 0.71$, where α is the molecular orbital coefficient of the ground state, indicating a moderate ($\sim$30%) contribution from the oxygen orbitals.

The electrochemical characterization of **1** can be divided in two potential domains. In the first domain, the Cu^{2+} reduction pattern in this complex closely resembles that of $CuSO_4$ under identical experimental conditions. A two-step reduction of Cu^{2+} to Cu^0 through Cu^+ was observed, with the expected modulation in potential locations due to the difference in ligands. It is noteworthy that all of the Cu^{2+} centers in **1** are electroactive. Reduction of the W framework started in a more negative potential domain. The accumulation of Cu^{2+} centers in **1** was found to be very beneficial for the electrocatalytic reduction of NO_x, including nitrate, nitrite, and N_2O. In the case of nitrate reduction, the observed efficiency was much higher than that obtained previously with Cu sandwich-type POMs. To our knowledge, **1** constitutes the first example of electrocatalysis of the reduction of N_2O by a POM.

The MS results illustrate the utility of the high resolution and ion handling ability of the FT-ICR mass analyzer applied to large POM species in solution. The accurate assignment of the molecular weight of the solution-phase species and the oxidation states of the W and Cu atoms in these species allow the characterization of a chemically useful system as well as the study of reactions in progress. IRMPD MS/MS of **1** allows the investigation of the stability of the metal oxide lattice in the absence of solvent effects. The observed fragments yield insight into the formation mechanism by identifying the most stable segments of **1**. The observation of fragmentation products similar to species previously observed during thermal decomposition and solution chemistry of POMs suggest that IRMPD generates chemically relevant fragments that improve the understanding of the structure and formation mechanisms of these species.

A salient feature of this work is the utilization of several structural characterization techniques to probe the chemistry of transition-metal-substituted POMs. Each technique provides complementary information, with FT MS as the newly introduced methodology. Here XRD provides fundamental knowledge of the polyanion structure and bonding of the overall lattice. Electrochemistry demonstrates the structural integrity of polyanion **1** in solution and elucidates its redox properties and electrocatalytic potential. Magnetization and EPR techniques reveal the magnetic properties of the material, interpretable on the basis of the structural and electrochemical oxidation state information. The exchange constants, EPR g values, and hyperfine parameters were interpreted according to the bonding parameters from the X-ray data, in turn enabling us to deduce the molecular orbital description of the unpaired electron in the Cu_5 moiety of **1**. Finally, FT-ICR MS provides a measurement of the molecular weight and total charge of isolated polyanion species in the gas phase. That information complements the structural and compositional data for **1** obtained from single-crystal XRD in the solid state, the reduction potentials from electrochemical measurements in solution, and the spin states from EPR in the solid state. Therefore, FT-ICR MS provides new information on possible changes to the polyanion structure that accompany the transition from solution to the gas phase. IRMPD MS/MS experiments in the gas phase shed light on the relative thermodynamic stability of the structural components in polyanion **1**. The observed structural and charge stability of the copper−hydroxo cluster in **1** is consistent with the CV results in solution, and the structure degradation patterns observed are consistent with those previously reported for thermal conversion of similar POM structures during bronze formation in the solid state. The apparent consistency of the degradation mechanism of **1** suggests that the observed fragmentation results from intrinsic polyanion properties and that solid-state or solvent effects are probably negligible.

Acknowledgment. This work was supported by the International University Bremen, the CNRS (UMR 8000), and the Université Paris-Sud XI. Florida State University thanks the National Science Foundation (NIRT; Grants DMR 0103290 and CHE-99-09502) for support. Figure 1 was generated by Diamond Version 3.0d (copyright Crystal Impact GbR).

Appendix

A. Basis Functions. The spin wave functions for the pentamer Cu_5 are derived from the basis set $|Ms_1, Ms_2, Ms_3, Ms_4, Ms_5\rangle$, where Ms_i is the microstate corresponding to the i^{th}

ion. Because each Cu^{2+} has $S_i = {}^1/_2$, Ms_i can take $+{}^1/_2$, $-{}^1/_2$ and from here onward this is represented respectively as $+$, $-$. Because the Ms_T values corresponding to the total spin S_T is $Ms_T = \Sigma_{i=1}^{5} Ms_i$, we have $Ms_T = \pm{}^5/_2$, $\pm{}^3/_2$, and $\pm{}^1/_2$. The possible linear combinations of Ms_i would give the complete set of eigenfunctions $\emptyset_i$.

$$
\begin{array}{cc}
Ms_T = {}^5/_2 & Ms_T = -{}^5/_2 \\
|+,+,+,+,+\rangle = \emptyset_1 & |-,-,-,-,-\rangle = \emptyset_{32} \\
Ms_T = {}^3/_2 & Ms_T = -{}^3/_2 \\
|-,+,+,+,+\rangle = \emptyset_2 & |+,-,-,-,-\rangle = \emptyset_{27} \\
|+,-,+,+,+\rangle = \emptyset_3 & |-,+,-,-,-\rangle = \emptyset_{28} \\
|+,+,-,+,+\rangle = \emptyset_4 & |-,-,+,-,-\rangle = \emptyset_{29} \\
|+,+,+,-,+\rangle = \emptyset_5 & |-,-,-,+,-\rangle = \emptyset_{30} \\
|+,+,+,+,-\rangle = \emptyset_6 & |-,-,-,-,+\rangle = \emptyset_{31} \\
Ms_T = {}^1/_2 & Ms_T = -{}^1/_2 \\
|-,-,+,+,+\rangle = \emptyset_7 & |+,+,-,-,-\rangle = \emptyset_{17} \\
|-,+,-,+,+\rangle = \emptyset_8 & |+,-,+,-,-\rangle = \emptyset_{18} \\
|-,+,+,-,+\rangle = \emptyset_9 & |+,-,-,+,-\rangle = \emptyset_{19} \\
|-,+,+,+,-\rangle = \emptyset_{10} & |+,-,-,-,+\rangle = \emptyset_{20} \\
|+,-,-,+,+\rangle = \emptyset_{11} & |-,+,+,-,-\rangle = \emptyset_{21} \\
|+,-,+,-,+\rangle = \emptyset_{12} & |-,+,-,+,-\rangle = \emptyset_{22} \\
|+,-,+,+,-\rangle = \emptyset_{13} & |-,+,-,-,+\rangle = \emptyset_{23} \\
|+,+,-,-,+\rangle = \emptyset_{14} & |-,-,+,+,-\rangle = \emptyset_{24} \\
|+,+,-,+,-\rangle = \emptyset_{15} & |-,-,+,-,+\rangle = \emptyset_{25} \\
|+,+,+,-,-\rangle = \emptyset_{16} & |-,-,-,+,+\rangle = \emptyset_{26}
\end{array}
$$

B. Exchange Matrix (32 × 32). The expanded form of the spin-exchange Hamiltonian given in eq 2 is:

$$
\begin{aligned}
\hat{H}_{\text{exch}} = -2J_a[(\hat{S}_{1x}\hat{S}_{2x} + \hat{S}_{1y}\hat{S}_{2y} + \hat{S}_{1z}\hat{S}_{2z}) + (\hat{S}_{3x}\hat{S}_{4x} + \\
\hat{S}_{3y}\hat{S}_{4y} + \hat{S}_{3z}\hat{S}_{4z})] - 2J_b[(\hat{S}_{1x}\hat{S}_{3x} + \hat{S}_{1y}\hat{S}_{3y} + \hat{S}_{1z}\hat{S}_{3z}) + \\
(\hat{S}_{2x}\hat{S}_{4x} + \hat{S}_{2y}\hat{S}_{4y} + \hat{S}_{2z}\hat{S}_{4z})] - 2J_c[(\hat{S}_{1x}\hat{S}_{5x} + \hat{S}_{1y}\hat{S}_{5y} + \\
\hat{S}_{1z}\hat{S}_{5z}) + (\hat{S}_{2x}\hat{S}_{5x} + \hat{S}_{2y}\hat{S}_{5y} + \hat{S}_{2z}\hat{S}_{5z}) + (\hat{S}_{3x}\hat{S}_{5x} + \hat{S}_{3y}\hat{S}_{5y} + \\
\hat{S}_{3z}\hat{S}_{5z}) + (\hat{S}_{4x}\hat{S}_{5x} + \hat{S}_{4y}\hat{S}_{5y} + \hat{S}_{4z}\hat{S}_{5z})] \quad \text{(B.1)}
\end{aligned}
$$

From the relations $\hat{S}_x = (\hat{S}^+ + \hat{S}^-)/2$ and $\hat{S}_y = (\hat{S}^+ - \hat{S}^-)/2i$, the Hamiltonian in eq B.1 can be rewritten as:

$$
\begin{aligned}
\hat{H}_{\text{exch}} = -2J_a[(\hat{S}_{1z}\hat{S}_{2z}) + (\hat{S}_1{}^+\hat{S}_2{}^- + \hat{S}_1{}^-\hat{S}_2{}^+) + (\hat{S}_{3z}\hat{S}_{4z}) + \\
(\hat{S}_3{}^+\hat{S}_4{}^- + \hat{S}_3{}^-\hat{S}_4{}^+)] - 2J_b[(\hat{S}_{1z}\hat{S}_{3z}) + (\hat{S}_1{}^+\hat{S}_3{}^- + \hat{S}_1{}^-\hat{S}_3{}^+) + \\
(\hat{S}_{2z}\hat{S}_{4z}) + (\hat{S}_2{}^+\hat{S}_4{}^- + \hat{S}_2{}^-\hat{S}_4{}^+)] - 2J_c[(\hat{S}_{1z}\hat{S}_{5z}) + (\hat{S}_1{}^+\hat{S}_5{}^- + \\
\hat{S}_1{}^-\hat{S}_5{}^+) + (\hat{S}_{2z}\hat{S}_{5z}) + (\hat{S}_2{}^+\hat{S}_5{}^- + \hat{S}_2{}^-\hat{S}_5{}^+) + (\hat{S}_{3z}\hat{S}_{5z}) + \\
(\hat{S}_3{}^+\hat{S}_5{}^- + \hat{S}_3{}^-\hat{S}_5{}^+) + (\hat{S}_{4z}\hat{S}_{5z}) + (\hat{S}_4{}^+\hat{S}_5{}^- + \hat{S}_4{}^-\hat{S}_5{}^+)] \quad \text{(B.2)}
\end{aligned}
$$

The exchange matrix corresponding to the Hamiltonian in eq B.2 with the matrix elements $\langle \emptyset_i | \hat{H}_{\text{exch}} | \emptyset_j \rangle$ can then be constructed as:

	$\emptyset_1$	$\emptyset_2$	$\emptyset_3$	$\emptyset_4$	$\emptyset_5$	$\emptyset_6$	$\emptyset_7$	$\emptyset_8$	$\emptyset_9$	$\emptyset_{10}$	$\emptyset_{11}$	$\emptyset_{12}$	$\emptyset_{13}$	$\emptyset_{14}$	$\emptyset_{15}$	$\emptyset_{16}$
$\emptyset_1$	α	−c	−a	−b	0	−c	δ	0	−b	−c	−b	0	−c	0	0	0
$\emptyset_2$	−c	−a	−c	0	−b	−c	0	ε	−a	−c	−a	0	0	0	−c	0
$\emptyset_3$	−a	−c	0	−b	−c		−b	−a	γ	−c	0	−a	0	−b	0	−c
$\emptyset_4$	−b	0	−c	−a	−c		−c	−c	−c	c	0	0	−a	0	−b	0
$\emptyset_5$	0	−b	−a	−c	−c		−b	−a	0	0	γ	−a	−c	−b	−c	0
$\emptyset_6$	−c	−c	−c	−c	β		0	0	−a	0	−a	ε	−c	0	0	−c
							−c	0	0	−a	−c	−c	c	0	0	−b
							0	0	−b	0	−b	0	0	δ	−c	−c
							0	−c	0	−b	−c	0	0	−c	c	−a
							0	0	−c	0	0	−c	−b	−c	−a	c

	$\emptyset_{17}$	$\emptyset_{18}$	$\emptyset_{19}$	$\emptyset_{20}$	$\emptyset_{21}$	$\emptyset_{22}$	$\emptyset_{23}$	$\emptyset_{24}$	$\emptyset_{25}$	$\emptyset_{26}$	$\emptyset_{27}$	$\emptyset_{28}$	$\emptyset_{29}$	$\emptyset_{30}$	$\emptyset_{31}$	$\emptyset_{32}$
$\emptyset_{17}$	δ	0	−b	−c	−b	0	−c	0	0	0	−c	−a	−b	0	−c	
$\emptyset_{18}$	0	ε	−a	−c	−a	0	0	0	−c	0	−a	−c	0	−b	−c	
$\emptyset_{19}$	−b	−a	γ	−c	0	−a	0	−b	0	−c	−b	0	−c	−a	−c	
$\emptyset_{20}$	−c	−c	−c	c	0	0	−a	0	−b	0	0	0	−a	−c	−c	
$\emptyset_{21}$	−b	−a	0	0	γ	−a	−c	−b	−c	0	−a	−c	−b	−c	0	
$\emptyset_{22}$	0	0	−a	0	−a	ε	−c	0	0	−c	−c	0	0	−c	0	
$\emptyset_{23}$	−c	0	0	−a	−c	−c	c	0	0	−b	0	−b	0	0	−b	
$\emptyset_{24}$	0	0	−b	0	−b	0	0	δ	−c	−c	−b	0	−b	0	0	
$\emptyset_{25}$	0	−c	0	−b	−c	0	0	−c	c	−a	0	−b	0	0	−b	
$\emptyset_{26}$	0	0	−c	0	0	−c	−b	−c	−a	c	−c	0	0	0	0	
$\emptyset_{27}$											−c	−a	−b	0	−c	
$\emptyset_{28}$											−a	−c	0	−b	−c	
$\emptyset_{29}$											−b	0	−c	−a	−c	
$\emptyset_{30}$											0	−b	−a	−c	−c	
$\emptyset_{31}$											−c	−c	−c	−c	β	
$\emptyset_{32}$																α

where $\boldsymbol{\alpha} = -J_a - J_a - 2J_c$, $\boldsymbol{\beta} = 2J_c - J_a - J_b$, $\boldsymbol{\delta} = -J_a + J_b$, $\boldsymbol{\epsilon} = J_a - J_b$, $\boldsymbol{\gamma} = J_a + J_b$, $\mathbf{a} = J_a$, $\mathbf{b} = J_b$, and $\mathbf{c} = J_c$. The eigenvalues of the above given exchange matrix are listed in Table 2.

Supporting Information Available: Table S1 shows the catalytic efficiencies for the electrocatalytic reduction of nitrate by **1** compared to Cu sandwich-type POMs, Figure S1 shows the CV of **1** extended to show the hydrogen evolution reaction wave just negative of the second W wave, and Figure S2 shows electrocatalysis of the reduction of nitrite in the presence of **1**. Complete X-ray crystallographic data for **K-1** (CIF format) are also provided. This material is available free of charge via the Internet at http://pubs.acs.org.

IC0512633